

High-Bandwidth Combinational Rogowski Coil for SiC MOSFET Power Module

Wen Zhang , *Member, IEEE*, Sadia Binte Sohid , Fred Wang, *Fellow, IEEE*, Helen Cui ,
and Bernhard Holzinger , *Associate Member, IEEE*

Abstract—Existing current sensors suffer from insufficient measurement bandwidth or large insertion area to faithfully capture the continuous switching transient current of wide-bandgap devices. The combinational Rogowski coil concept is proposed here, where the self-integrating region of a shielded Rogowski coil is combined with its differentiating region to extend the overall measurement bandwidth. The coil design methodology, including the parasitic element model and practical design boundaries, is discussed. The concept is implemented with printed circuit boards and prototypes demonstrated up to 300 MHz bandwidth. The coil can also be easily integrated in an SiC MOSFET module power stage and it is shown that the switching transient current waveform is faithfully captured.

Index Terms—Current sensor, double pulse test, measurement bandwidth, Rogowski coil, wide-bandgap devices.

I. INTRODUCTION

THE current measurement and monitoring technique is critical for understanding and modeling the switching devices. SiC devices exhibit much faster switching capability and smaller parasitic capacitances than Si counterparts [1]. Furthermore, recent packaging technique improvements have enabled smaller and smaller power loop inductance for SiC MOSFET modules [2], [3]. The switching transient oscillation frequency determined by the parasitic capacitance and inductance is therefore greatly increased. In order to capture the current waveform faithfully, the current sensor or probe must possess sufficiently high measurement bandwidth. Furthermore, the switching transient behavior of SiC MOSFETs is sensitive to the power loop parasitic inductance [4]. However, threading the power loop current through a current sensor invariably results in a larger power loop area. The

resulting extra power loop inductance must be kept as small as possible.

There are several high-bandwidth current measurement techniques [5]. Resistive current shunts can achieve very high bandwidth up to several GHz but cannot achieve high bandwidth, small footprint, and continuous current conduction at the same time [6], [7]. Current transformers can achieve up to 250 MHz measurement bandwidth but the cross-sectional area is quite large due to the magnetic material saturation limitation [8]. The resulting extra power loop area when routing the power loop conductor around the current transformer is therefore also large. Rogowski coils are another widely used type of current sensor based on Faraday's induction law [9]. The helix coil directly measures the derivative of the current, which is then reconstructed by a passive or active integrating circuit [10]. The state-of-the-art commercial Rogowski coil has a small circular cross-sectional area with a diameter of 3.5 mm but the measurement bandwidth is limited to 50 MHz [11]. Most of the recent Rogowski coil designs for power electronics application share the same concept, which uses an external integrator circuit to integrate the current derivative signal from the coil [12]. A Rogowski coil with up to 225 MHz bandwidth is demonstrated in [13], but numerical integration with oscilloscope is required and the sensitivity is quite low due to the low number of turns. Wang *et al.* [14] proposed an integrated Rogowski coil for a GaN power stage but the measurement bandwidth is not explicitly given. PCB-based Rogowski coils have also been used for diode switching energy measurement but the bandwidth is limited to around tens of MHz [15]. Attempts have also been made to integrate PCB Rogowski coils into the SiC MOSFET power stage [16]. Following the same integrating the differentiating region concept, the bandwidth is limited to 28.3 MHz.

On the other hand, the lesser used self-integrating Rogowski coils can exhibit linear instead of differentiating output with respect to the measured current [17]. Instead of a single return turn going through the center of the coil, a layer of copper shielding covers the entire coil from outside, as shown in Fig. 1. In this simplified schematic, the circular helix winding is wrapped around with insulating and shielding material. The coil is terminated between one end of the winding and the shielding. The other end of the winding is connected to the shielding. The parasitic capacitance between the coil winding and the shielding can achieve passive integration in the high frequency range [10], [18], with higher bandwidth up to hundreds of MHz. However, in the aforementioned literature, the coils are quite large whose

Manuscript received June 7, 2021; revised August 26, 2021 and October 20, 2021; accepted November 9, 2021. Date of publication November 12, 2021; date of current version December 31, 2021. This work was supported in part by Keysight Technologies through CURENT industry membership, in part by the Engineering Research Program of the National Science Foundation, in part by the Department of Energy under NSF Grant EEC-1041877, and in part by the CURENT Industry Partnership Program. Recommended for publication by Associate Editor M. Hartmann. (*Corresponding author: Wen Zhang.*)

Wen Zhang, Sadia Binte Sohid, Fred Wang, and Helen Cui are with the Department of Electrical Engineering and Computer Science, University of Tennessee Knoxville, Knoxville, TN 37996 USA (e-mail: wzhang53@vols.utk.edu; ssohid@vols.utk.edu; fred.wang@utk.edu; helencui@utk.edu).

Bernhard Holzinger is with Keysight Technologies Deutschland GmbH, 71034 Böblingen, Germany (e-mail: bernhard_holzinger@keysight.com).

Color versions of one or more figures in this article are available at <https://doi.org/10.1109/TPEL.2021.3127545>.

Digital Object Identifier 10.1109/TPEL.2021.3127545

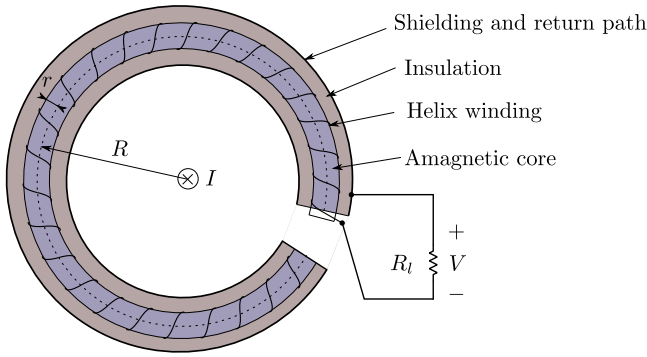


Fig. 1. Simplified schematic of a shielded Rogowski coil.

diameters are at least in tens of millimeters. Therefore, they are also not suitable for SiC MOSFET measurement.

In our previous work [19], a combinational Rogowski coil concept is proposed, which utilizes both the self-integrating and differentiating characteristics of a shielded Rogowski coil. However, the implementation was hand-made and not controllable. In this article, the coil is implemented on printed circuit boards (PCBs) and can be easily integrated into the switching power stage. The measurement bandwidth is greatly increased, while the cross-sectional area is kept small to minimize the extra power loop inductance. The design methodology and practical considerations are also provided, including the parasitic element model and error analysis. Network analyzer measurements verify the measurement bandwidth of experimental prototypes can be up to 300 MHz. SiC MOSFET module double pulse tests with either standalone or integrated combinational Rogowski coil power stage further shows the coil can faithfully capture the switching transient current.

II. COMBINATIONAL ROGOWSKI COIL CONCEPT

A. Shielded Coil Characteristics

Assuming the parasitic inductance and capacitance are evenly distributed along the coil, the equivalent distributed element circuit model for a shielded Rogowski coil is shown in Fig. 2. The turn-to-turn capacitance and ac winding resistance are neglected to simplify the analysis. The inductance L_p represents the primary-side conductor carrying the measured current. The coil is terminated with a load resistance of R_l . The coil self inductance is denoted as L_s . The winding to shielding capacitance is denoted as C_g . And the mutual inductance between the primary side conductor and the coil is denoted as M . The superscript prime represents the per-unit-length value in Fig. 2. The transfer impedance from the input current I and the output voltage V is given by [17]

$$Z_t = \frac{V}{I} = \frac{M}{L_s} \cdot \frac{1}{R_l^{-1} - jZ_0^{-1} \cot(\omega\sqrt{L_s C_g})} \quad (1)$$

where $Z_0 = \sqrt{\frac{L_s}{C_g}}$ is the wave impedance of the coil. Note that the relationship is derived by neglecting the turn-to-turn capacitance. This is justified by the small number of turns used

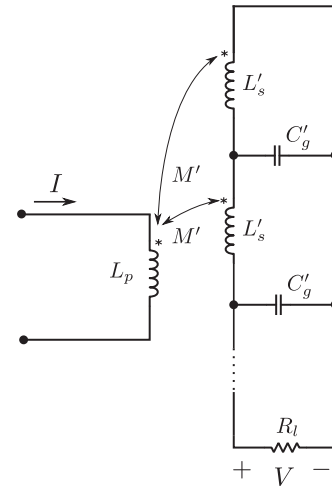


Fig. 2. Simplified distributed element circuit model of a shielded Rogowski coil assuming all elements are evenly distributed.

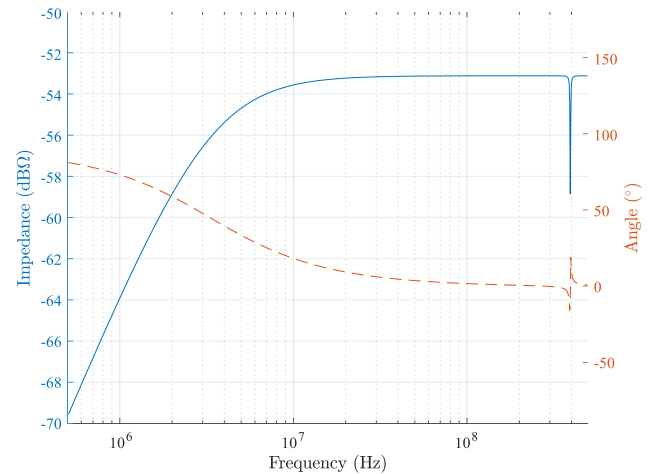


Fig. 3. Modeled transfer impedance of Rogowski coil design #1.

in the later prototypes. The turn-to-turn capacitance is typically very small and less than 1 fF when number of turns is small [17].

A transfer impedance example over the frequency spectrum is shown in Fig. 3. The transfer impedance clearly shows distinctive behaviors in different frequency regions. In the lower frequency spectrum, the coil appears differentiating. The gain increases at a rate of 20 dB/decade and the phase angle is at 90° . Inspecting (1), when $Z_0^{-1} \cot(\omega\sqrt{L_s C_g}) \gg R_l^{-1}$, the coil output behaves as a typical Rogowski coil

$$Z_t \approx j\omega M. \quad (2)$$

From 3 to 400 MHz, Fig. 3 shows that the coil output becomes linear. From (1), when $Z_0^{-1} \cot(\omega\sqrt{L_s C_g}) \ll R_l^{-1}$, the output of the coil will be proportional to the primary-side current and appears linear or self-integrating

$$Z_t \approx \frac{R_l M}{L_s}. \quad (3)$$

Because of the periodic nature of the cot function, the linear response region appears in many high frequency bands. The first

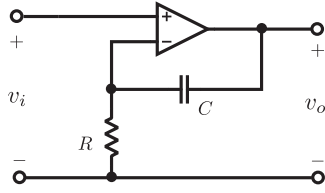


Fig. 4. Analog signal processing circuit for the combinational Rogowski coil which has integrating behavior in the low frequency and linear output in the high frequency.

frequency band immediately after the differentiating region can be used for the current sensing purpose. The primary-side current signal starts being distorted at the first oscillation point, and the rest of high-frequency spectrum response cannot be used to reconstruct the current signal. The lower and higher frequencies of the first self-integrating band can be found by equating the previous frequency band conditions

$$BW_L = \frac{\arctan \frac{R_l}{Z_0}}{2\pi\sqrt{L_s C_g}} \quad (4)$$

$$BW_H = \frac{\pi - \arctan \frac{R_l}{Z_0}}{2\pi\sqrt{L_s C_g}}. \quad (5)$$

In the example shown in Fig. 3, $BW_L \approx 3$ MHz and $BW_H \approx 400$ MHz. In fact, typically the coils are designed so that $BW_H \gg BW_L$ and we can leverage the self-integrating region to extend the bandwidth. Therefore, we have $\arctan \frac{R_l}{Z_0} \ll \pi$ and the bandwidth expressions can be further simplified

$$BW_L \approx \frac{R_l}{2\pi L_s} \quad (6)$$

$$BW_H \approx \frac{1}{2\sqrt{L_s C_g}}. \quad (7)$$

B. Combinational Rogowski Coil

The combinational Rogowski coil concept here measures the current signal by utilizing both the differentiating and self-integrating region. The differentiating region below BW_L is integrated by an integrator circuit. And the self-integrating region above BW_L is directly fed to the output. Corresponding to the coil behavior, the analog signal processing circuit must exactly match the transition frequency BW_L , below which it appears integrating and above which it appears linear. A possible analog signal processing circuit candidate is shown in Fig. 4. It is trivial to see the transfer function for this simple noninverting integrator circuit is

$$\frac{v_o}{v_i} = 1 + \frac{1}{sRC}. \quad (8)$$

Therefore, to have a flat measured current to output voltage response, we have

$$BW_L = \frac{1}{2\pi RC}. \quad (9)$$

Because the integrator circuit has unity gain beyond BW_L , the overall sensor gain is clearly determined by the linear gain

in the self-integrating region, as given in (3). From (3), (6), and (7), it is trivial to see that the load resistance R_l determines the overall gain and the lower self-integrating frequency. A smaller load resistance R_l means a lower gain and a lower transition frequency BW_L . The higher bandwidth BW_H , however, is only dependent on the natural oscillation frequency of the Rogowski coil. Therefore, it is beneficial to minimize the parasitic elements to achieve the highest possible BW_H . Note, however, the performance of the analog signal processing circuit in (8) is ultimately limited by the op-amp's bandwidth. This means the overall higher bandwidth is also limited by the choice of op-amp.

C. Coil Hardware Implementation

As alluded previously, it is beneficial to create a small coil for higher BW_H . The experimental prototypes are therefore built on PCBs with down to 3 mil spacing. The coil implementation approach on the PCB is shown in Fig. 5. The coil is built on a four-layer PCB. The helix winding is woven in the middle two layers. Buried vias between these two layers are used to connect the traces. The major and minor radius of the winding is denoted as R and r , respectively. The winding height h_c is determined by the distance between the middle layers. The top and bottom layers act as the shielding layers. Full-stack vias are used to connect the shielding together. The insulation height h_s between the winding and shielding is again determined by the PCB stack up. The load resistance is connected directly to the winding terminal and the shielding. An SubMiniature version A (SMA) connector is then connected in parallel to feed the signal to the analog signal processing circuit.

III. COIL MODELS AND PRACTICAL CONSIDERATIONS

A. Parasitic Element Model

Because the shielded Rogowski coil's performance is solely determined by its parasitic elements, analytical models for these elements can greatly facilitate the coil design optimization. Given the Rogowski coil shape in Fig. 5, the mutual inductance M_0 between the primary-side conductor and the coil is given by

$$M_0 = \frac{\mu_0}{2\pi} N h_c \log \frac{R+r}{R-r} \quad (10)$$

where N is the number of turns, and h_c is the winding height and the same as the distance between the PCB inner layers.

The per-unit-length winding-to-shielding capacitance C'_g can be approximated by the asymmetrical stripline capacitance [20]

$$C'_g = \frac{1.10 \times 10^{-10} \epsilon_r}{\ln \frac{2(2h_s+h_c)}{0.268w+0.335t}} \text{ (pF/m)} \quad (11)$$

where w and t are the width and thickness of the PCB winding copper trace, respectively, and ϵ_r is the relative permittivity of the PCB substrate material.

The parasitic inductance L'_s is more convoluted. Dubickas and Edin [17] argue there are two independent contributions of inductance which are the wire-over-ground-plane inductance L'_1 and the helix-winding inductance L'_2 for circular shielded

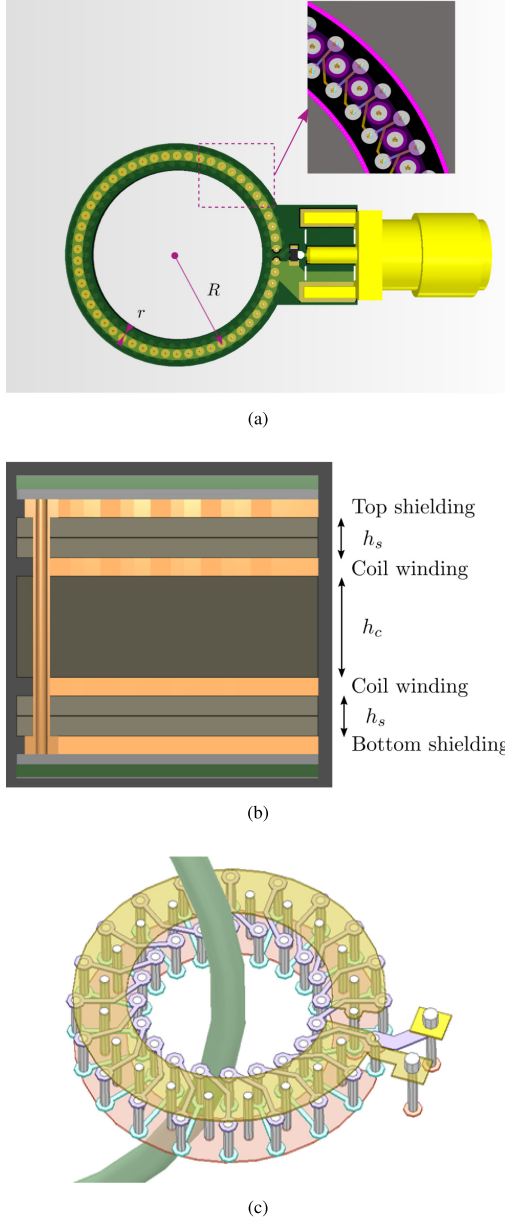


Fig. 5. Shielded Rogowski coil PCB design. (a) PCB geometry and winding layout with coil design #1. (b) PCB layer stackup. (c) Q3D extractor model showing PCB trace routing and vias with coil design #2.

Rogowski coils. Similarly, the first part can be calculated by [20]

$$Z_s = \frac{80}{\epsilon_r} \left[1 - \frac{h_s}{4(h_s + h_c)} \right] \cdot \ln \frac{1.9(2h_s + t)}{0.8w + t} \quad (12)$$

$$L'_1 = C'_g Z_s^2. \quad (13)$$

The second part can be written as

$$L_2 = \frac{\mu_0}{2\pi} N^2 h_c \ln \frac{R + r}{R - r}. \quad (14)$$

Then the self-inductance L'_s can be calculated by $L'_s = L'_1 + L'_2$. However, the assumption that these two inductances are independent and orthogonal may not be true. As the frequency increases, the magnetic field distribution inside the coil will



Fig. 6. Tilted primary-side conductor in Rogowski coil.

crowd between the winding and shielding due to the ac proximity effect. Therefore, the calculated self-inductance L'_s may be overestimating, especially in the high frequencies. This means the linear gain, transition frequency BW_L , and higher frequency BW_H will all be underestimated.

B. Mutual Inductance Error Analysis

Given the implementation approach and parasitic element model in the previous section, it is already possible to formulate an optimization problem on the coil design. However, just like conventional differentiating Rogowski coils, the mutual inductance suffers from eccentric and tilting errors because of nonuniform or sparse winding [21].

Ideally, the primary-side conductor is placed at the center of the Rogowski coil and goes through it perpendicularly to the coil plane. However, in reality, the primary-side conductor can be tilted and at an angle θ against the normal of the coil plane, as shown in Fig. 6. Following the similar derivation process in [21], the actual mutual inductance M can be found by summing the mutual inductance of each turn, and the expression is given in (15), where $\alpha = \frac{2\pi}{N}$ represents the spanning angle of each turn.

Assuming the major radius $R = 7.0$ mm, the minor radius $r = 0.5$ mm, and the coil height $h_c = 0.2$ mm, numerical calculation gives us the variation of mutual inductance M when the primary-side conductor is tilted and sweeping the total number of turns N . The numerical sweeping result is shown in Fig. 7. When the tilting angle θ is small, there is little difference between the actual mutual inductance M and the ideal mutual inductance M_0 . However, when the primary-side conductor is tilted toward 90° , the change in mutual inductance is particularly significant when the number of turns N is small. This means to achieve a consistent measurement for different tilting angle, the winding density should be as dense as possible.

Another nonideal condition is when the primary-side conductor is eccentric and placed at a distance of ΔR to the center of the coil, as shown in Fig. 8. Likewise, following the derivation process in [21], the actual mutual inductance M is found by summing the mutual inductance of each turn, and the expression is given in (16). Similarly, having the winding as dense as possible clearly results in a more consistent measurement.

In summary, like a traditional Rogowski coil, the winding density must be sufficiently dense to ensure the mutual inductance is consistent, no matter where the primary-side conductor

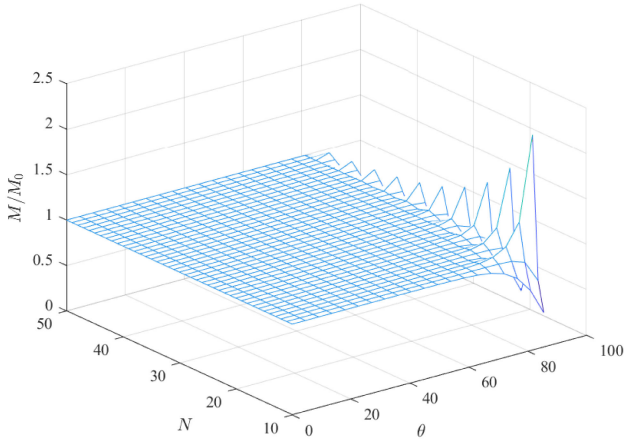


Fig. 7. Variation of mutual inductance M when primary-side conductor is tilted with different number of turns N .

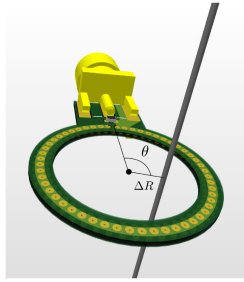


Fig. 8. Eccentric primary-side conductor in Rogowski coil.

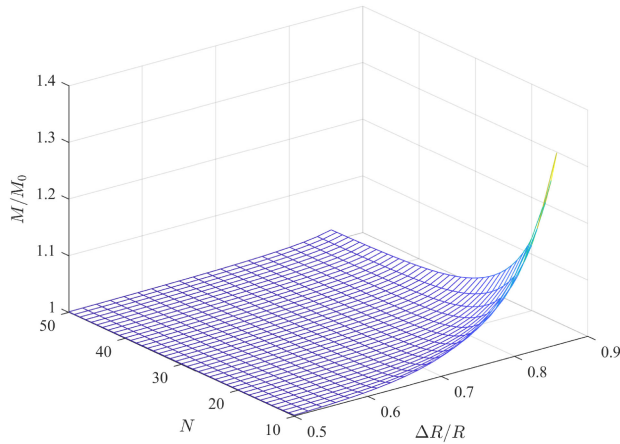


Fig. 9. Variation of mutual inductance M when primary-side conductor is eccentric with different number of turns N .

is placed. The above analysis provides a design boundary for the number of turns N , as shown in Fig. 9. In the given example, $N > 45$ to ensure the maximum mutual inductance error is less than 5.0%.

$$M = \frac{\mu_0 h_c}{2\pi} \ln \left(\frac{R+r}{R-r} \right) \times \sum_{i=1}^N \frac{\cos \theta}{\sqrt{1 - \sin^2 \theta \sin^2 i\alpha} \cdot \sqrt{\sin^2 \theta \cos^2 i\alpha + \cos^2 \theta}} \quad (15)$$

TABLE I
COMBINATIONAL ROGOWSKI COIL #1 DESIGN PARAMETERS

Parameter	Value
No. of Turns N	54
Major Radius R	7.50 mm
Minor Radius r	0.50 mm
Coil Height h_c	0.20 mm
Shielding Height h_s	0.08 mm
Copper thickness	1.0 oz
Trace width	3.0 mil
Load Resistance R_l	0.50 Ω

$$M = \frac{\mu_0 h_c}{2\pi} \sum_{i=1}^N \ln \left(\frac{R^2 + \Delta R^2 - 2R\Delta R \cos i\alpha + Rr - \Delta Rr \cos i\alpha}{R^2 + \Delta R^2 - 2R\Delta R \cos i\alpha - Rr + \Delta Rr \cos i\alpha} \right). \quad (16)$$

C. High-Frequency Behavior Distortion

Note that in Fig. 2, it is assumed that each segment of the distributed circuit shares the same per-unit-length parameters. While this is true for the self-inductance L'_s and winding-to-shielding capacitance C'_g , the mutual inductance M' distribution becomes uneven when the primary-side conductor is not at its ideal location. To illustrate the impact of uneven mutual inductance distribution, the primary-side conductor is assumed eccentric here. The mutual inductance of each turn is first calculated. The distributed circuit model SPICE netlist is then automatically generated with a script, where each turn is modeled as a single segment. The parameters of the coil design used for analysis are shown in Table I.

Following the notation in Fig. 8, the variation in transfer impedance with different eccentric angle θ and eccentric distance ΔR is shown in Fig. 10. In Fig. 10(a), the primary-side conductor is placed perpendicularly at the center of the coil, and the high-frequency behavior is exactly the ideal case, as shown in Fig. 3, with higher measurement bandwidth at around 400 MHz. However, as the primary-side conductor moves away from the center, as shown in Fig. 10(a) and (b), where $\Delta R = 0$ and $\Delta R = 0.8R$, respectively, the high-frequency behavior becomes distorted. The distortion appears most significant when the primary-side conductor is placed at $\theta = 90^\circ$ with respect to the terminal of the coil. As shown in Fig. 10(c), when $\Delta R = 0.8R$, the distortion at the first resonance is a lot more severe and the usable measurement bandwidth (± 3 dB) is reduced to around 300 MHz.

The analysis here clearly shows the high-frequency behavior is also subject to variation when the primary-side conductor is not at its ideal location. This means the actual usable bandwidth is lower than the designed value, and enough bandwidth margin must be kept to ensure the final bandwidth is sufficient. On the other hand, it also suggests that if applicable, the primary-side conductor should be located ideally at the dead center of the coil. It is later shown that it is trivial to do so when embedding the coil in the switching power stage. Finally, this also means the coil winding must be evenly distributed; otherwise, the unevenly

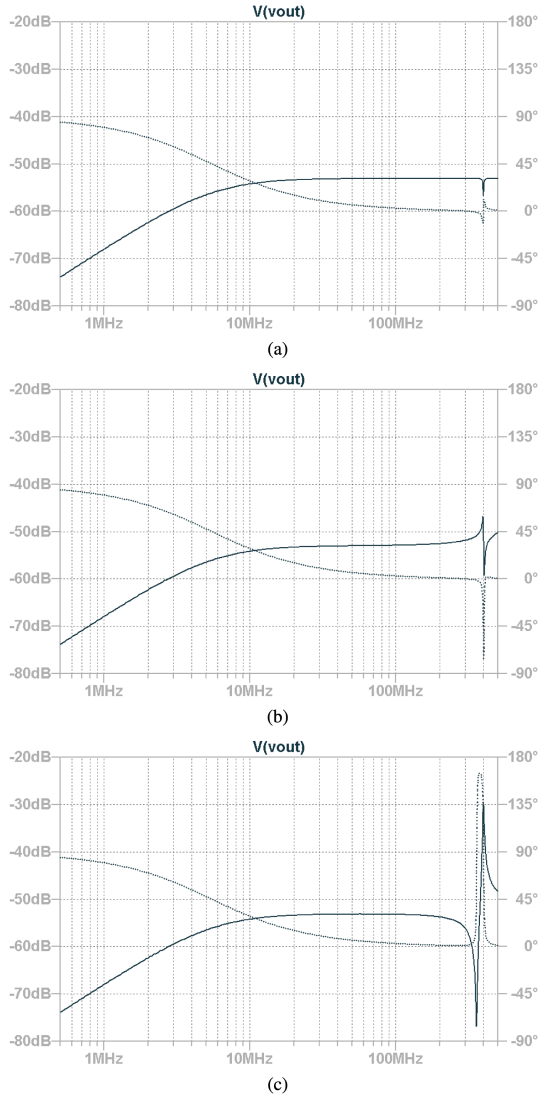


Fig. 10. Rogowski coil #1 high-frequency distortion due to high-frequency distortion. (a) $\theta = 0^\circ$ and $\Delta R = 0$. (b) $\theta = 180^\circ$ and $\Delta R = 0.8R$. (c) $\theta = 90^\circ$ and $\Delta R = 0.8R$.

distributed mutual inductance would distort the high-frequency behavior.

IV. COIL DESIGNS AND PERFORMANCE VERIFICATION

A. Coil High-Frequency Performance Measurement

Two experimental prototypes are built and tested. The modeled transfer impedance of the first prototype coil #1 is shown in Fig. 3 and the coil design parameters are listed in Table I. The sensitivity or gain is around $-53.0 \text{ dB}\Omega$ or $2.2 \text{ m}\Omega$, which is more suitable for higher current measurement. The modeled transfer impedance of the second prototype coil #2 is shown in Fig. 11 and the coil design parameters are listed in Table II. The sensitivity is around $-36.3 \text{ dB}\Omega$ or $15.3 \text{ m}\Omega$. Compared with coil #1, #2 is much smaller with a major radius of only 2.0 mm. The upper self-integrating bandwidth according to the model is also a lot higher, beyond 500 MHz. As such, #2 is more suitable to measuring lower current devices.

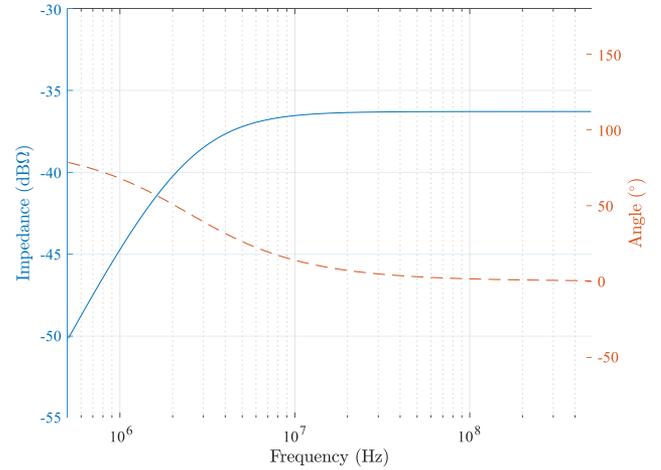
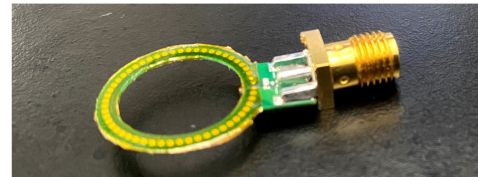


Fig. 11. Modeled transfer impedance of combinational Rogowski coil design #2.

TABLE II
COMBINATIONAL ROGOWSKI COIL #2 DESIGN PARAMETERS

Parameter	Value
No. of Turns N	20
Major Radius R	2.00 mm
Minor Radius r	0.50 mm
Coil Height h_c	0.80 mm
Shielding Height h_s	0.11 mm
Copper thickness	1.0 oz
Trace width	3.0 mil
Load Resistance R_l	0.50Ω



(a)



(b)

Fig. 12. Combinational Rogowski coil prototypes. (a) Coil #1 built on 0.40-mm PCB. (b) Coil #2 built on 1.20-mm PCB.

Both prototypes are shown in Fig. 12. Coil #2 is very small, with the whole coil smaller than the SMA connector. The measurement setup is also illustrated with the coil #2. An SMA cable is striped near its end and the center conductor is bent to create a small loop and shorted to the external ground shielding. The small loop is wrapped around the coil to act as the primary-side conductor. The shorted cable is connected to port 1 of a network analyzer and the coil output is connected to port 2. The network analyzer used here is the Keysight E5061B, sweeping from 500 kHz to 500 MHz. The transfer impedance Z_t can be obtained

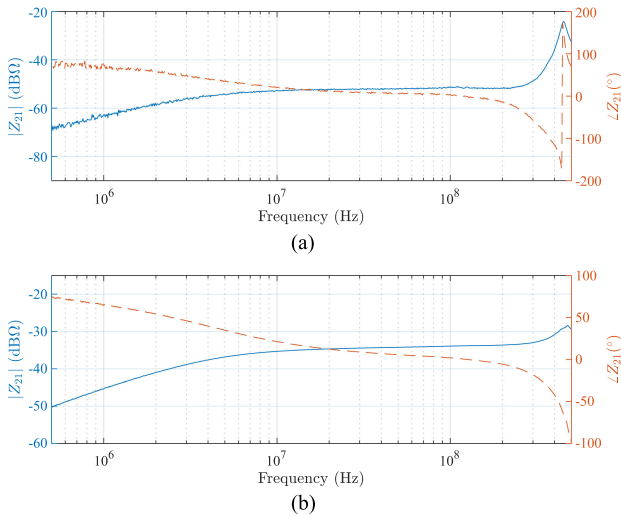


Fig. 13. High-frequency network analyzer measurement result with the combinational Rogowski coils only. (a) Coil #1. (b) Coil #2.

by converting from the S -parameter measurement result

$$Z_t = \frac{2S_{12}}{(1 - S_{11})(1 - S_{22}) - S_{12}S_{21}} Z_o \quad (17)$$

where $Z_o = 50 \Omega$.

The measurement results of both coils are shown in Fig. 13. Following the discussion on high-frequency behavior distortion, the measurement setup is essentially the worst case for the mutual inductance uneven distribution. The primary-side conductor loop has the strongest coupling with the turn it immediately encircled. As expected, the high-frequency distortion is quite significant in both coils. Nevertheless, the usable measurement bandwidth (± 3 dB) for coil #1 is around 300 MHz and for coil #2 is around 382 MHz. The measurement result of coil #1 also appears more noisy. This is because the gain of the coil is much lower than coil #2. The high-frequency response is not completely flat for both coils, which is probably because of the high-frequency ac resistance impact. Comparing the measurement result to the model prediction in Figs. 3 and 11, both the transition frequency BW_L and the gain Z_t are higher than the model. Like previously discussed, this is expected since the self-inductance L'_s calculation tends to overestimate its value.

B. Overall Behavior With Analog Signal Processing Circuit

The analog signal processing circuit is implemented with LTC6228, which has a rail-to-rail output. The power supply for the op-amp is ± 5.0 V. As an example, the overall performance of coil #2 is shown with the integrator circuit. The overall high-frequency response is measured in the same way as the coil-only high frequency response. The primary-side conductor made from the SMA cable short loop is connected to port 1. The Rogowski coil is connected with the integrator input terminal, and the integrator output is directly fed to port 2 of network analyzer. The measurement result is shown in Fig. 14. The op-amp circuit further created some high-frequency distortion, and its high-frequency response is not particularly flat and the overall measurement bandwidth is reduced to around 300 MHz. Also

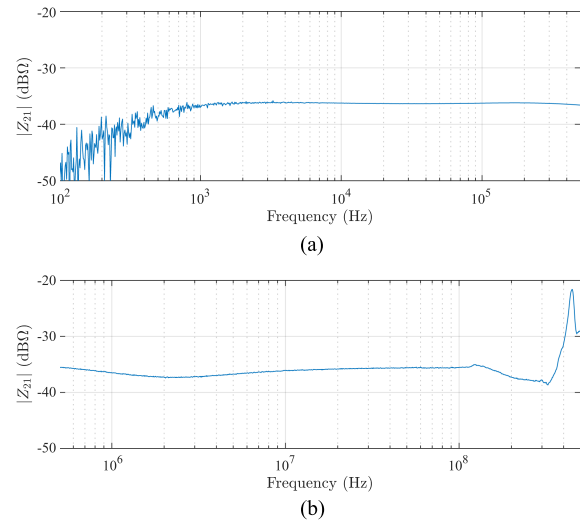


Fig. 14. Transfer impedance measurement of coil #2 with signal processing circuit. (a) Low frequency. (b) High frequency.

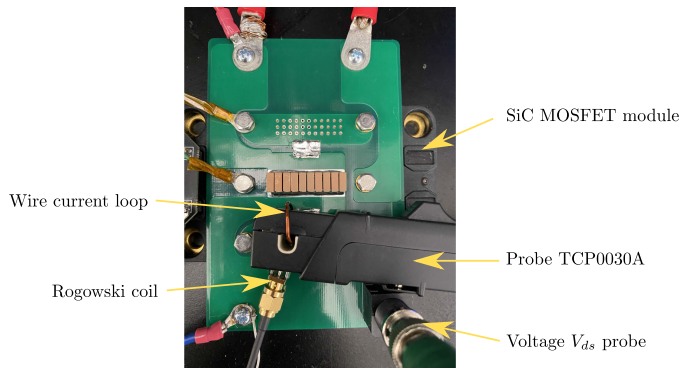


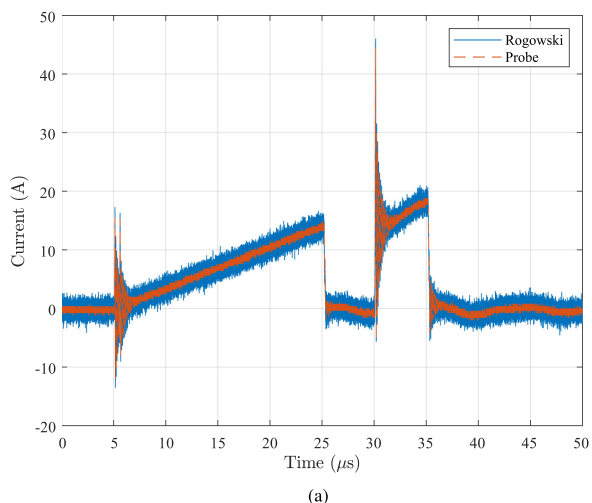
Fig. 15. Standalone Rogowski coil #1 double pulse test setup to compare it with commercial current probe.

note that at around the transition frequency of around 4 MHz, the gain is not very flat. This is likely due to the integrator circuit component mismatch. Nevertheless, the concept here is verified and the integrator circuit directly outputs the high-frequency components of the Rogowski coil.

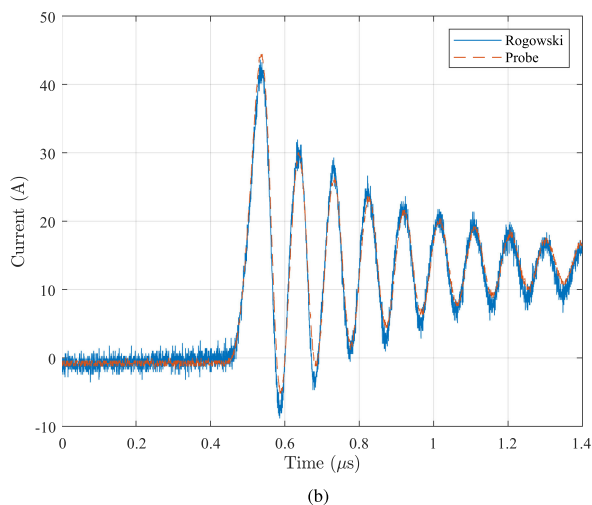
The lower frequency response between 100 Hz and 500 kHz is measured with the gain/phase measurement on the Keysight E5061B. The measurement result is also shown in Fig. 14. The sensor exhibits a very flat response from around 400 Hz all the way to 500 kHz. Therefore, the analog signal processing circuit works as intended, integrating all the low-frequency components. The measurement below 1 kHz is particularly noisy, though, likely because of the op-amp circuit intrinsic noise or the network analyzer's limited resolution for very low bandwidth measurement. Below 400 Hz, the gain is increasing at a rate of 20 dB/dec. This is because of the limited op-amp gain at lower frequencies to suppress low-frequency noise.

C. Double Pulse Test With Standalone Coil

The coil #1 is tested in a standalone fashion, and the test setup with SiC MOSFET module CAS325M12HM2 which is rated at 1200 V and around 400 A. As a comparison between



(a)

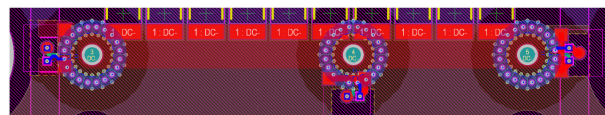


(b)

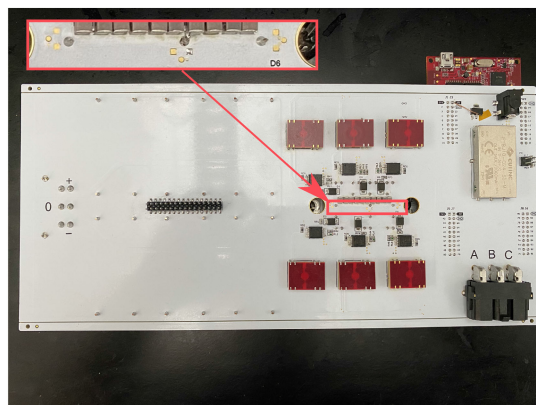
Fig. 16. Double pulse test waveform comparison between standalone Rogowski coil #1 and commercial current probe. (a) Overall. (b) Turn-ON transient.

the commercial current probe TCP0030 A (50 A, 120 MHz) and the Rogowski coil, the measurement setup deliberately created a large loop in the switching power loop, as shown in Fig. 15. The Rogowski coil is hidden under the commercial current probe.

Because of the large power loop and the limited 50 A maximum current capability of TCP0030 A, the double pulse test was performed at relatively low voltage and current. The waveform comparison is shown in Fig. 16. The Rogowski coil current signal is converted from the oscilloscope voltage reading of the integrator circuit. The sensitivity is obtained from the network analyzer measurement result. Because of the relatively low current and the low sensitivity of coil #1, the measurement noise is relatively significant in the Rogowski coil. The turn-ON transient comparison between them shows nearly the same measurement result in the rising edge and the oscillation afterwards. Therefore, it is proved the combinational Rogowski coil concept works as intended.



(a)



(b)

Fig. 17. Integrated Rogowski coil #2 double pulse test setup with SiC MOSFET module CCB021M12FM3. (a) PCB layout. (b) Hardware setup highlighting the location of the coils.

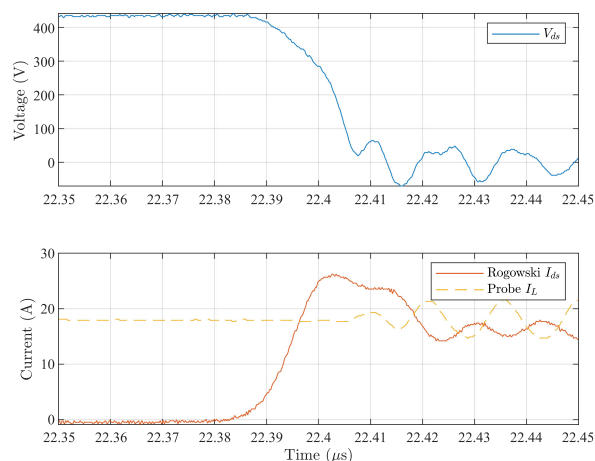


Fig. 18. Turn-ON transient voltage and current waveform in the integrated Rogowski coil double pulse test.

D. Double Pulse Test With Integrated Coil

To further demonstrate the capability of integrating the coil into the PCB design and achieving the optimal power stage layout, the coil #2 design is embedded into the switching power stage for SiC MOSFET module CCB021M12FM3, which is rated at 1200 V and around 50 A. The PCB layout is shown in Fig. 17(a). The PCB design uses six layers with a total thickness of 2.0 mm. The third to sixth layers share the same stackup as coil #2 in Table II. The same coil winding and vias are used in these four layers. The hardware setup is shown in Fig. 17(b). MMCX connectors are used to feed the integrated coil voltage to the off-board integrator circuit. The turn-ON transient voltage and current waveform is shown in Fig. 18. Because of the compact

layout, the current probe is only measuring the load current. The switching transient oscillation frequency is around 79 MHz. With the integrated Rogowski coil, the turn-ON transient waveforms are captured faithfully with negligible interference into the power loop.

V. CONCLUSION

The combinational Rogowski coil concept is proposed here. The self-integrating characteristics of shielded Rogowski coils can be utilized to extend the overall measurement bandwidth. The design methodology and practical considerations are provided. The parasitic element models can facilitate the design, while the error and distortion analysis define the design boundary considerations. Experimental prototypes built with PCB demonstrate a measurement bandwidth of more than 300 MHz. The integrated power stage also shows that the concept provides a non-invasive approach for measuring and monitoring the SiC devices switching transient current of SiC devices. The combinational Rogowski coil here is also a promising technique to build a standalone current probe for more general-purpose use, given its high bandwidth and small profile.

REFERENCES

- [1] J. Biela, M. Schweizer, S. Waffler, and J. W. Kolar, "SiC versus Si - Evaluation of potentials for performance improvement of inverter and DC-DC converter systems by SiC power semiconductors," *IEEE Trans. Ind. Electron.*, vol. 58, no. 7, pp. 2872–2882, Jul. 2011.
- [2] Z. Huang *et al.*, "A novel low inductive 3D SiC power module based on hybrid packaging and integration method," in *Proc. IEEE Energy Convers. Congr. Expo.*, 2017, pp. 3995–4002.
- [3] F. Hou *et al.*, "Review of packaging schemes for power module," *IEEE Trans. Emerg. Sel. Topics Power Electron.*, vol. 8, no. 1, pp. 223–238, Mar. 2020.
- [4] Z. Chen, D. Boroyevich, and R. Burgos, "Experimental parametric study of the parasitic inductance influence on MOSFET switching characteristics," in *Proc. IEEE Conf. Int. Power Electron.*, 2010, pp. 164–169.
- [5] S. Ziegler, R. C. Woodward, H. H.-C. Lu, and L. J. Borle, "Current sensing techniques: A review," *IEEE Sensors J.*, vol. 9, no. 4, pp. 354–376, Apr. 2009.
- [6] W. Zhang, Z. Zhang, F. Wang, E. V. Brush, and N. Forcier, "High-bandwidth low-inductance current shunt for wide-bandgap devices dynamic characterization," *IEEE Trans. Power Electron.*, vol. 36, no. 4, pp. 4522–4531, Apr. 2021.
- [7] T&M Research, "Current viewing resistors," 2021. [Online]. Available: <http://www.tandmresearch.com/>
- [8] Pearson Electronics, "Pearson current monitor," 2021. [Online]. Available: <https://www.pearsonelectronics.com/pdf/7713-03.pdf>
- [9] W. Rogowski and W. Steinhaus, "Die messung der magnetischen spannung," *Archiv für Elektrotechnik*, vol. 1, no. 4, pp. 141–150, 1912.
- [10] M. H. Samimi, A. Mahari, M. A. Farahnakian, and H. Mohseni, "The Rogowski coil principles and applications: A review," *IEEE Sensors J.*, vol. 15, no. 2, pp. 651–658, Feb. 2015.
- [11] Power Electronics Measurement, "CWT MiniHF," 2021. [Online]. Available: <http://pemuk.com>
- [12] Y. Shi, Z. Xin, P. C. Loh, and F. Blaabjerg, "A review of traditional helical to recent miniaturized printed circuit board Rogowski coils for power-electronic applications," *IEEE Trans. Power Electron.*, vol. 35, no. 11, pp. 12207–12222, Nov. 2020.
- [13] J. Wang *et al.*, "Infinity sensor: Temperature sensing in GaN power devices using Peak di/dt," in *Proc. IEEE Energy Conv. Congr. Expo.*, 2018, pp. 884–890.
- [14] K. Wang, X. Yang, H. Li, L. Wang, and P. Jain, "A high-bandwidth integrated current measurement for detecting switching current of fast GaN devices," *IEEE Trans. Power Electron.*, vol. 33, no. 7, pp. 6199–6210, Jul. 2018.
- [15] F. Naseri, E. Farjah, and T. Ghanbari, "Application of an efficient Rogowski coil sensor for online estimation of turn-off energy loss of power diodes," *IEEE Sensors J.*, vol. 19, no. 16, pp. 6675–6683, Aug. 2019.
- [16] J. Wang, S. Mocevic, R. Burgos, and D. Boroyevich, "High-scalability enhanced gate drivers for SiC MOSFET modules with transient immunity beyond 100 V/ns," *IEEE Trans. Power Electron.*, vol. 35, no. 10, pp. 10180–10199, Oct. 2020.
- [17] V. Dubickas and H. Edin, "High-frequency model of the Rogowski coil with a small number of turns," *IEEE Trans. Instrum. Meas.*, vol. 56, no. 6, pp. 2284–2288, Dec. 2007.
- [18] I. A. Metwally, "Self-integrating Rogowski coil for high-impulse current measurement," *IEEE Trans. Instrum. Meas.*, vol. 59, no. 2, pp. 353–360, Feb. 2010.
- [19] W. Zhang, F. Wang, and B. Holzinger, "High-bandwidth shielded Rogowski coil current sensor for SiC MOSFET power module," in *Proc. IEEE Conf. Appl. Power Electron. Conf. Expo.*, 2021, pp. 1242–1249.
- [20] H. W. Johnson, M. Graham, and Others, *High-Speed Digital Design: A Handbook of Black Magic*, vol. 155. Englewood Cliffs, NJ, USA: Prentice Hall, 1993.
- [21] G. Zhang and Y. Liu, "Positional error analysis of PCB Rogowski coil for high accuracy current measurement," *Adv. Mech. Eng.*, vol. 5, 2013, Art. no. 375301.